

# Nondestructive quantitative synchrotron grazing incidence X-ray scattering analysis of cylindrical nanostructures in supported thin films

Jinhwan Yoon,<sup>a‡</sup> Seung Yun Yang,<sup>b‡</sup> Byeongdu Lee,<sup>c</sup> Wonchul Joo,<sup>b</sup>  
Kyuyoung Heo,<sup>a</sup> Jin Kon Kim<sup>b\*</sup> and Moonhor Ree<sup>a\*</sup>

<sup>a</sup>National Research Laboratory for Polymer Synthesis and Physics, Department of Chemistry, Pohang Accelerator Laboratory, Center for Integrated Molecular Systems, and BK School of Molecular Science, Pohang University of Science and Technology, Pohang 790-784, Republic of Korea, <sup>b</sup>National Creative Research Initiative Center for Block Copolymer Self-Assembly, Department of Chemical Engineering and School of Environmental Science and Engineering, Pohang University of Science and Technology, Pohang 790-784, Republic of Korea, and <sup>c</sup>Experimental Facility Division, Argonne National Laboratory, Argonne, IL 60439, USA. Correspondence e-mail: jkkim@postech.edu, ree@postech.edu

Nondestructive nanostructural analysis is indispensable in the development of nanomaterials and nanofabrication processes for use in nanotechnology applications. This paper demonstrates a quantitative, nondestructive analysis of nanostructured thin films supported on substrates and their templated nanopores by using grazing incidence X-ray scattering and data analysis with a derived scattering theory. The analysis disclosed that vertically oriented nanodomain cylinders had formed in 20–100 nm thick films supported on substrates, which consisted of a mixture of poly(styrene-*b*-methyl methacrylate) (PS-*b*-PMMA) and PMMA homopolymer, and that the PMMA nanodomain cylinders were selectively etched out by ultraviolet light exposure and a subsequent rinse with acetic acid, resulting in a well ordered nanostructure consisting of hexagonally packed cylindrical nanopores.

© 2007 International Union of Crystallography  
Printed in Singapore – all rights reserved

## 1. Introduction

Template methods have been extensively employed in nanotechnology in applications ranging from new catalysts, quantum dots, metal or metal oxide (and even conductive polymer) nanowires, and carbon nanotubes, to enzymatic bioreactors and membranes for biomaterials (Meneou *et al.*, 2005; Wang *et al.*, 2004; Wu *et al.*, 2004; Miller *et al.*, 2001; Lakshmi & Martin, 1997). Among these templates, block copolymer nanotemplates consisting of cylindrical microdomains oriented vertically on a substrate have received significant attention (Yang *et al.*, 2006; Park *et al.*, 2003; Thurn-Albrecht *et al.*, 2000). The cylindrical microdomains of one component of the block copolymer are removed by UV irradiation and a subsequent rinse with a solvent, generating cylindrical nanoporous templates (Jeong *et al.*, 2004). In general, the size and the shape of the nanopores in a template directly control the shape and properties of the final product, and thus quantitative analysis of the pores, including their shape, size, size distribution, orientation and ordering, is essential. For instance, the preparation of cylindrical nanopores in a polycarbonate membrane track-etched with high-

energy particle irradiation has been reported (Lakshmi & Martin, 1997). However, the detailed structures of such nanopores cannot easily be determined *a priori* until metal wires grown inside the nanopores are examined by transmission and scanning electron microscopy (TEM and SEM).

Microscopy techniques such as TEM, SEM and atomic force microscopy (AFM) have been widely used to explore nanostructures. However, TEM and SEM are destructive methods, particularly in the preparation of sample specimens, so extreme care is required in sample preparation to avoid damaging the samples, especially for nanotemplates fabricated from soft or polymeric materials. When the nanopores are placed on a substrate, as in anodized aluminium oxide membranes (Meneou *et al.*, 2005) or nanoporous structures prepared from block copolymer thin films on silicon substrates (Yang *et al.*, 2006; Park *et al.*, 2003; Jeong *et al.*, 2004; Thurn-Albrecht *et al.*, 2000), the preparation of the specimens and analysis of the nanopores with TEM and SEM are extremely difficult. Furthermore, the regions of the specimens that are accessible with these types of microscopy are quite limited. Although AFM is a very powerful tool for the examination of surface topography, it cannot be used to investigate nanostructures underneath the surface. To determine the large-scale features of template nanostructures, conventional

‡ J. Yoon and S. Y. Yang contributed equally to this work.

transmission neutron and X-ray scattering (TNS and TXS) have also been widely used (Lee *et al.*, 2004; Sakurai *et al.*, 1998). However, these scattering techniques are not applicable to nanotemplates supported with substrates or in supported thin films because of their low sensitivity and resolution, which arise for low scattering volumes and when the substrates are much thicker than the nanostructures (Lee, Oh, Yoon *et al.*, 2005). Thus, a nondestructive method is required for the quantitative analysis of nanotemplates supported with substrates or in supported thin films.

In this paper we describe a nondestructive grazing incidence X-ray scattering (GIXS) technique, which can produce a high intensity scattering pattern with high statistical significance even for thin films with a thickness of tens of nanometres that are supported with substrates (Chung *et al.*, 2006; Kim *et al.*, 2006; Lee, Oh, Hwang *et al.*, 2005; Lee, Oh, Yoon *et al.*, 2005; Lee, Park, Yoon *et al.*, 2005; Lee, Park, Hwang *et al.*, 2005; Lee, Yoon *et al.*, 2005). However, the use of the GIXS technique is only possible in conjunction with scattering theory development and intensive data analysis because grazing incidence scattering is complicated by reflection and refraction effects (Busch *et al.*, 2006; Park *et al.*, 2005; Lee, Oh, Hwang *et al.*, 2005; Lee, Oh, Yoon *et al.*, 2005; Lee, Park, Yoon *et al.*, 2005; Lee, Park, Hwang *et al.*, 2005; Lee, Yoon *et al.*, 2005; Omote *et al.*, 2003; Holy *et al.*, 1999; Tolan, 1999; Sinha *et al.*, 1988) that are not found in conventional TXS and TNS. Because of these complexities of GIXS data analysis, the full use of the power of GIXS in the characterization of nanostructure systems, such as block copolymer thin films with various morphologies and their nanotemplates, has been limited.

In this study, we fabricated cylindrical nanostructures in thin films by using poly(styrene-*b*-methyl methacrylate) (PS-*b*-PMMA; volume fraction of the PMMA block  $f_{\text{PMMA}} = 0.25$ , weight-average molecular weight  $\overline{M}_w = 73\,000$ , and polydispersity index  $\text{PDI} = 1.06$ ) mixed with a small amount of PMMA homopolymer ( $\overline{M}_w = 31\,800$  and  $\text{PDI} = 1.08$ ), and investigated the nanostructures before and after selective etching of the phase-separated PMMA microdomains with the aid of UV light irradiation and a subsequent rinse with acetic acid (this process is henceforth called ‘UV-etching’) by using GIXS with synchrotron X-ray radiation sources. For the analysis of the GIXS data, we derived a GIXS formula. The GIXS measurements and the quantitative data analysis using the derived GIXS formula were found to provide important structural details and properties of the thin films and their nanoporous templates that cannot be obtained with conventional microscopic and scattering methods.

## 2. Theory

### 2.1. GIXS formula for cylindrical nanostructures

The intensity of GIXS ( $I_{\text{GIXS}}$ ) from a thin film of the PS-*b*-PMMA/PMMA mixture supported with a substrate can be expressed as the scattering formula derived recently (Lee, Park, Yoon *et al.*, 2005; Lee, Yoon *et al.*, 2005):

$$I_{\text{GIXS}}(\alpha_f, 2\theta_f) \cong \frac{1}{16\pi^2} \frac{1 - \exp[-2\text{Im}(q_z)d]}{2\text{Im}(q_z)} \times \left\{ |T_i T_f|^2 I_1[q_{\parallel}, \text{Re}(q_{1,z})] + |T_i R_f|^2 I_1[q_{\parallel}, \text{Re}(q_{2,z})] + |T_f R_i|^2 I_1[q_{\parallel}, \text{Re}(q_{3,z})] + |R_i R_f|^2 I_1[q_{\parallel}, \text{Re}(q_{4,z})] \right\}, \quad (1)$$

where  $\text{Im}(q_z) = |\text{Im}(k_{z,f})| + |\text{Im}(k_{z,i})|$ ,  $\text{Re}(x)$  is the real part of  $x$ ,  $d$  is the film thickness,  $R_i$  and  $T_i$  are the reflected and transmitted amplitudes of the incoming X-ray beam, respectively, and  $R_f$  and  $T_f$  are the reflected and transmitted amplitudes of the outgoing X-ray beam, respectively. In addition,  $q_{\parallel} = (q_x^2 + q_y^2)^{1/2}$ ,  $q_{1,z} = k_{z,f} - k_{z,i}$ ,  $q_{2,z} = -k_{z,f} - k_{z,i}$ ,  $q_{3,z} = k_{z,f} + k_{z,i}$  and  $q_{4,z} = -k_{z,f} + k_{z,i}$ ; here,  $k_{z,i}$  is the  $z$  component of the wavevector of the incoming X-ray beam, which is given by  $k_{z,i} = k_0(n_R^2 - \cos^2 \alpha_i)^{1/2}$ , and  $k_{z,f}$  is the  $z$  component of the wavevector of the outgoing X-ray beam, which is given by  $k_{z,f} = k_0(n_R^2 - \cos^2 \alpha_f)^{1/2}$ , where  $k_0 = 2\pi/\lambda$ ,  $\lambda$  is the wavelength of the X-ray beam,  $n_R$  is the refractive index of the film given by  $n_R = 1 - \delta + i\xi$  with dispersion  $\delta$  and absorption  $\xi$ ,  $\alpha_i$  is the out-of-plane grazing incident angle of the incoming X-ray beam, and  $\alpha_f$  is the out-of-plane exit angle of the outgoing X-ray beam.  $q_x$ ,  $q_y$ , and  $q_z$  are the components of the scattering vector  $\mathbf{q}$ .  $I_1$  is the scattering intensity of the phase-separated microdomains or templated nanopores in the film.

In equation (1),  $I_1$  is the scattered intensity from microdomains formed in the mixture film, and thus can be expressed by the following equation (Lee, Park, Yoon *et al.*, 2005; Pedersen, 1994):

$$I_1(\mathbf{q}) = P(\mathbf{q}) \cdot S(\mathbf{q}), \quad (2)$$

where  $P(\mathbf{q})$  is the form factor of the microdomains that describes the shape, size and orientations of the microdomains, and  $S(\mathbf{q})$  is the structure factor that provides information on the positions of the microdomains such as the crystal lattice parameters, orientation, dimensions and symmetry in an ordered structure.

Here we consider a cylindrical scatterer in taking into account the AFM and SEM images of the films, which suggest that the PMMA microdomains developed in the films have a cylindrical shape. The form factor  $P(\mathbf{q})$  for the cylinder of radius  $R$  and length  $L$  can be expressed as follows (Pedersen, 1997; Fournet, 1951):

$$P(\mathbf{q}) = F^2(\mathbf{q}, R, L), \quad (3)$$

where  $F(\mathbf{q}, R, L)$  is the structure amplitude of the cylindrical scatterer given by

$$F(\mathbf{q}, R, L) = 2\pi R^2 L \frac{J_1(q_{\parallel} R)}{q_{\parallel} R} \frac{\sin(q_z L/2)}{q_z L/2} \exp(-iq_z L/2). \quad (4)$$

Here it is assumed that the distribution of the radius  $R$  of the cylindrical particles follows a Gaussian distribution size distribution function  $G(R)$ :

$$G(R) = \frac{1}{(2\pi)^{1/2} \sigma_R} \exp\left[-\frac{(R - \overline{R})^2}{2\sigma_R^2}\right], \quad (5)$$

where  $\bar{R}$  and  $\sigma_R$  are the mean radius and the standard deviation of  $R$  from  $\bar{R}$ , respectively. The size distribution of the cylindrical particles can be taken into account by averaging the form factor  $\langle F \rangle$  with respect to  $R$ , yielding

$$\langle F \rangle = \frac{\int_0^\infty G(R)F(q, R, L) dR}{\int_0^\infty G(R) dR}. \quad (6)$$

For a paracrystalline lattice consisting of cylinders, the structure factor  $S(\mathbf{q})$  (the so-called interference function or lattice factor) can be determined from the Fourier transform of a complete set of lattice points (Busson & Doucet, 2000; Hashimoto *et al.*, 1994; Hosemann & Bagchi, 1962). In a paracrystal with distortion of the second kind, the positions of the lattice points can only be described with a positional distribution function. In the simple case where the auto-correlation function of the crystal lattice is given by the convolution product of the distributions of the lattice points along three axes, and the distribution function is a Gaussian,  $S(\mathbf{q})$  can be expressed by the following equation:

$$S(\mathbf{q}) = \prod_{k=1}^3 Z_k(\mathbf{q}). \quad (7)$$

The  $k$ th lattice factor  $Z_k(\mathbf{q})$  is given by

$$Z_k(\mathbf{q}) = 1 + \frac{F_k(\mathbf{q})}{1 - F_k(\mathbf{q})} + \frac{F_k^*(\mathbf{q})}{1 - F_k^*(\mathbf{q})}, \quad (8)$$

where

$$F_k(\mathbf{q}) = |F_k(\mathbf{q})| \exp(-i\mathbf{q} \cdot \mathbf{b}_k) \quad (9)$$

and

$$|F_k(\mathbf{q})| = \exp(-g_k^2 q^2 \mathbf{b}_k^2 / 2). \quad (10)$$

Here,  $g_k$  are the components of the paracrystal distortion factor defined by

$$g_k^2 = \Delta^2 \mathbf{b}_k / \mathbf{b}_k^2, \quad (11)$$

where  $\mathbf{b}_k$  and  $\Delta \mathbf{b}_k$  are the fundamental vector of the  $k$ th axis and its displacement, respectively. In the present study, isotropic displacement is assumed and the domain orientation is accounted for numerically. For a thin film with a given orientation, its fundamental vectors can be rotated and transformed by a rotation matrix.

When the structure (for example, paracrystal in our study) in a thin film is randomly oriented in the plane of the film but uniaxially oriented out of plane, the peak position vector  $\mathbf{q}_c$  of a certain reciprocal lattice point  $\mathbf{c}^*$  in the sample reciprocal lattice is given by

$$\mathbf{q}_c = \mathbf{R} \cdot \mathbf{c}^* \equiv (q_{c,x}, q_{c,y}, q_{c,z}), \quad (12)$$

where  $\mathbf{R}$  is a  $3 \times 3$  matrix to decide the preferred orientation of the structure in the film, and  $q_{c,x}$ ,  $q_{c,y}$ ,  $q_{c,z}$  are the  $x$ ,  $y$ ,  $z$  components of the peak position vector  $\mathbf{q}_c$ , respectively. Using equation (12), every peak position can be obtained. Because of cylindrical symmetry, the Debye–Scherrer ring composed of

the in-plane randomly oriented  $\mathbf{c}^*$  cuts an Ewald sphere at two points in its top hemisphere:  $q_{\parallel} = q_{c,\parallel} \equiv \pm(q_{c,x}^2 + q_{c,y}^2)^{1/2}$ , with  $q_z = q_{c,z}$ . Thus diffraction patterns with cylindrical symmetry are easily calculated in the  $\mathbf{q}$  space. It is then convenient to determine the preferred orientation of known structures and further to analyze anisotropic X-ray scattering patterns. However, since  $\mathbf{q}$  space is distorted in GIXS by refraction and reflection effects, the relation between the detector plane expressed as the Cartesian coordinate defined by two perpendicular axes (*i.e.* by the in-plane exit angle  $2\theta_f$  and the out-of-plane exit angle  $\alpha_f$ ) and the reciprocal lattice points is needed. The two wavevectors  $k_{z,i}$  and  $k_{z,f}$  are corrected for refraction as  $k_o(n_R^2 - \cos^2 \alpha_i)^{1/2}$  and  $k_o(n_R^2 - \cos^2 \alpha_f)^{1/2}$ , respectively. Therefore, the two sets of diffractions that result from the incoming and outgoing X-ray beams, denoted by  $q_1$  and  $q_3$ , respectively, are given at the exit angles by the following expression:

$$\alpha_f = \arccos \left\{ n_R^2 - [q_{c,z}/k_o \pm (n_R^2 - \cos^2 \alpha_i)^{1/2}]^2 \right\}^{1/2}, \quad (13)$$

where  $q_{c,z}/k_o > (n_R^2 - \cos^2 \alpha_i)^{1/2}$ . In equation (13), the positive sign denotes diffractions produced by the outgoing X-ray beam, and the negative sign denotes diffractions produced by the incoming X-ray beam. The in-plane incidence angle  $2\theta_i$  is usually zero, so the in-plane exit angle  $2\theta_f$  can be expressed as follows:

$$2\theta_f = \arccos \left[ \frac{\cos^2 \alpha_i + \cos^2 \alpha_f - (q_{c,\parallel}/k_o)^2}{2 \cos \alpha_i \cos \alpha_f} \right]. \quad (14)$$

Therefore, diffraction spots detected on the detector plane in GIXS measurements can be directly compared with those derived using equations (12)–(14) from an appropriate model and thus analyzed in terms of the model.

## 2.2. Numerical analysis

Using the equations described in §2.1, we conducted numerical GIXS analyses for a thin film consisting of a hexagonal paracrystal lattice composed of cylinders that are randomly oriented in the plane of the film but uniaxially oriented out of the film plane, in order to determine the relationships between the film's structural parameters and the resulting GIXS pattern. Representative results are shown in Fig. 1.

Fig. 1(a) shows the effects of both the structure factor  $S(\mathbf{q})$  and the form factor  $P(\mathbf{q})$  on the GIXS intensity  $I_{\text{GIXS}}(\mathbf{q})$  along the in-plane axis of the film; in this calculation, hexagonally packed cylinders with  $d_{100} = 34.0$  nm,  $g = 0.03$ ,  $\bar{R} = 10.0$  nm and  $\sigma_R = 1.25$  nm were used. The structure factor  $S(\mathbf{q})$  contains diffraction peaks that are characteristic of the symmetry and space group of the hexagonally packed lattice; a different crystalline lattice would produce higher-order diffractions in different positions. The form factor  $P(\mathbf{q})$  of the cylinder leads to a  $q^{-4}$  decay in the Porod region, and produces damped oscillations with positions, periodicity and amplitude that are characteristic of the particle size, shape and polydispersity, respectively.

$I_{\text{GIXS}}(\mathbf{q})$  varies with the paracrystal distortion factor  $g$ , which is defined in equation (11). Fig. 1(b) shows the  $I_{\text{GIXS}}(\mathbf{q})$  profiles for hexagonally packed cylinders (which are defined by the paracrystalline parameters  $d_{100} = 34.0$  nm,  $\bar{R} = 11.5$  nm and  $\sigma_R = 1.15$  nm) with various  $g$  factors:  $g = 0.02, 0.04$  and  $0.06$ . In this calculation, isotropic distortion is assumed, and therefore the value of the  $g$  factor is independent of the displacement direction. In the case of  $g = 0.02$ , many sharp peaks appear, which are the characteristic diffractions of a hexagonal lattice. Some of these peaks were assigned to the (100), (110), (200), (210), (300), (220), (310) and (400) diffractions in the order of low to high  $q_{xy}$ , with relative scattering vector lengths from the specular reflection position of  $1, 3^{1/2}, 4^{1/2}, 7^{1/2}, 9^{1/2}, 12^{1/2}, 13^{1/2}$  and  $16^{1/2}$ , respectively. As the  $g$  factor increases, these diffraction peaks clearly become weaker and broader. Thus this kind of distortion decreases the amplitudes of the intensities of the Bragg diffraction peaks and increases the broadness of the diffraction peaks; such peak broadness is much more severe for higher-order diffraction peaks. In conclusion, the vectors of adjacent lattice cells vary in magnitude and direction because of the dis-

placements of the lattice points from their proper positions, ultimately resulting in a loss of long-range order in the paracrystal. Therefore,  $g$ -factor analysis can provide an experimental basis for determining the degree of lattice distortion in a paracrystalline system, and furthermore the lattice dimensions can be determined from the diffraction peak positions.

Fig. 1(c) shows the influence of the cylinder radius  $\bar{R}$  on  $I_{\text{GIXS}}(\mathbf{q})$  for hexagonally packed cylinders with  $d_{100} = 34.0$  nm,  $g = 0.03$  and  $\sigma_R/\bar{R} = 0.1$ ; in this calculation,  $\bar{R}$  varies in the range 5–15 nm. As can be seen in the figure,  $\bar{R}$  directly affects the positions of the peak maxima and minima. As a result, the relative intensities of the diffraction peaks are sensitive to variations in the radii of the cylinders. For example, as  $\bar{R}$  increases the minimum of the first peak shifts to the smaller  $q$  region and the minima of the higher-order peaks are damped (Fig. 1c). Thus this analysis provides a basis for the experimental determination of the radii of the cylinders and the deviation.

Fig. 1(d) shows profiles of  $I_{\text{GIXS}}(\mathbf{q})$  along the out-of-plane axis of the film, which were calculated by varying the cylinder length  $L$  for hexagonally packed cylinders with  $d_{100} = 34.0$  nm,  $g = 0.03$ ,  $\bar{R} = 10.0$  nm,  $\sigma_R = 1.25$  nm and  $\rho_{e,f}$  (electron density of the film) =  $260 \text{ nm}^{-3}$ . Since the incident angle  $\alpha_i$  is very small, the GIXS signal depends mainly on the in-plane scattering vector component  $q_{xy}$ , which is related to the lateral ordering in the film, and the out-of-plane scattering vector component  $q_z$ , which is related to the ordering in the thickness direction of the film. Here we assume that the cylinders in the film are perfectly oriented normal to the film plane, and thus that the  $I_{\text{GIXS}}(\mathbf{q})$  profile varies only with the cylinder length  $L$ . As can be seen in Fig. 1(d), as the cylinder length  $L$  increases the first minimum of the oscillation shifts to the smaller- $q_z$  region, and this effect is independent of the radius of the cylinders. Thus this analysis provides a basis for the experimental determination of the lengths of the cylinders.

As discussed above, the GIXS profile was found to be sensitive to all the structural parameters of  $P(\mathbf{q})$  and  $S(\mathbf{q})$ , namely the paracrystal lattice and dimensions, paracrystal distortion factor, cylinder orientation, cylinder radius and radius distribution, and cylinder length. These numerical analysis results demonstrate that the GIXS technique is a very powerful tool for the unambiguous determination of the structural parameters of nanostructures in thin films.

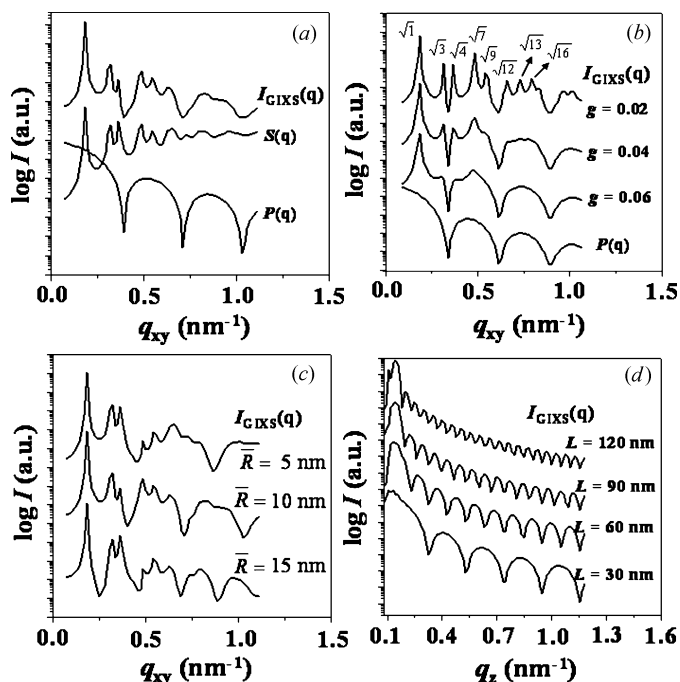


**Figure 1**  
 (a) In-plane GIXS profile  $I_{\text{GIXS}}(\mathbf{q})$ , structure factor  $S(\mathbf{q})$  and form factor  $P(\mathbf{q})$  calculated for a thin film with a hexagonally packed cylindrical paracrystalline structure oriented normal to the film plane; in these calculations, the structural parameters were  $d_{100} = 34.0$  nm,  $g = 0.03$ ,  $\bar{R} = 10.0$  nm and  $\sigma_R = 1.25$  nm. (b) The effect of the paracrystal distortion factor  $g$  on the in-plane  $I_{\text{GIXS}}(\mathbf{q})$  profile for a vertically oriented paracrystalline structure of hexagonally packed cylinders with  $d_{100} = 34.0$  nm,  $\bar{R} = 11.5$  nm and  $\sigma_R = 1.15$  nm. (c) The effect of the cylinder radius on the in-plane  $I_{\text{GIXS}}(\mathbf{q})$  profile for a vertically oriented paracrystalline structure of hexagonally packed cylinders with  $d_{100} = 34.0$  nm,  $g = 0.03$  and  $\sigma_R/\bar{R} = 0.1$ . (d) The effect of the cylinder length on the out-of-plane  $I_{\text{GIXS}}(\mathbf{q})$  profile at the diffraction angle of the first-order diffraction peak for a vertically oriented paracrystalline structure of hexagonally packed cylinders with  $d_{100} = 34.0$  nm,  $g = 0.03$ ,  $\bar{R} = 10.0$  nm,  $\sigma_R = 1.25$  nm and  $\rho_{e,f} = 260 \text{ nm}^{-3}$ .  $\rho_{e,f}$  is the electron density of the film.

### 3. Experiment

#### 3.1. Sample preparation

Asymmetric PS-*b*-PMMA ( $f_{\text{PMMA}} = 0.25$ ,  $\bar{M}_w = 73\,000$  and PDI = 1.06) was synthesized from styrene and methyl methacrylate monomers by atom transfer radical polymerization (Jeong *et al.*, 2004). A hydroxy end-functionalized random copolymer of styrene and methyl methacrylate, denoted PS-*r*-PMMA ( $f_{\text{PMMA}} = 0.60$ ), was synthesized in bulk *via* a 2,2,6,6-tetramethylpiperidinyloxy living free radical polymerization ( $\bar{M}_w = 9600$  and PDI = 1.80). An atactic PMMA homopolymer with  $\bar{M}_w = 31800$  and PDI = 1.08 was

purchased from Polymer Source. Two solutions of PS-*b*-PMMA ( $f_{\text{PMMA}} = 0.25$ ) containing 6.95% of the PMMA homopolymer with respect to the volume of the PMMA block in the diblock copolymer were prepared in toluene with concentrations of 1.0 and 2.0% (*w/v*). In addition, a 1.0% (*w/v*) PS-*r*-PMMA ( $f_{\text{PMMA}} = 0.60$ ) solution in toluene was prepared.

A neutral brush layer ( $\sim 6$  nm thick) was deposited on precleaned silicon substrates with a native oxide layer by spin-coating the PS-*r*-PMMA solution and drying in a vacuum oven at 443 K for 2 d. The mixture of PS-*b*-PMMA/PMMA was then deposited on the substrates by spin-coating and drying in a vacuum oven at 443 K for 2 d.

For some films, the PMMA phase (PMMA microdomains plus PMMA homopolymer) was etched out as follows. The film was exposed to the UV light ( $\lambda = 253.7$  nm) of a UV lamp (model G15T8, Sankyo Denki, Japan) for 90 min in a vacuum chamber, developed by immersion in acetic acid for 1 h at room temperature, and then finally rinsed several times with deionized water. The patterned films were dried in vacuum for 12 h at room temperature.

### 3.2. GIXS measurements

GIXS measurements were carried out at the 4C1 and 4C2 beamlines (Yu *et al.*, 2005; Bolze *et al.*, 2002) of the Pohang Accelerator Laboratory (Ree & Ko, 2005). The sample-to-detector distance was 2152 mm; an X-ray radiation source of  $\lambda = 0.154$  nm and a two-dimensional charge-coupled detector (two-dimensional CCD: Roper Scientific, Trenton, NJ, USA) were used. Samples were mounted on a four-circle goniometer (Huber, Rimsting, Germany) equipped with a vacuum chamber. The incidence angle of the X-ray beam was  $0.20^\circ$ , which is between the critical angles of the films and the silicon substrates. Scattering angles were corrected by the positions of X-ray beams reflected from the silicon substrate interface with changing incidence angle and by a precalibrated polystyrene-*b*-polyethylene-*b*-polybutadiene-*b*-polystyrene (SEBS) block copolymer standard. A set of aluminium foil strips were employed as semi-transparent beam stops because the intensity of the specular reflection from the substrate is much stronger than the intensity of GIXS near the critical angle. Data were collected for 10 s. In addition, the surfaces of the films were examined by using a tapping mode atomic force microscope (Digital Instruments, model Multimode AFM Nanoscope IIIa) and a field emission scanning electron microscope (FE-SEM, Hitachi S-4800). The cross sections of some etched films were additionally investigated by FE-SEM.

## 4. Results and discussion

Fig. 2(*a*) shows schematic pictures of the tens of nanometres thick nanostructure, prepared from a mixture of the PS-*b*-PMMA and the PMMA homopolymer, and the nanoporous template that was produced by the selective UV-etching of the phase-separated PMMA microdomains. The addition of the PMMA homopolymer was found to be necessary for obtaining vertically oriented cylindrical PMMA microdomains when the

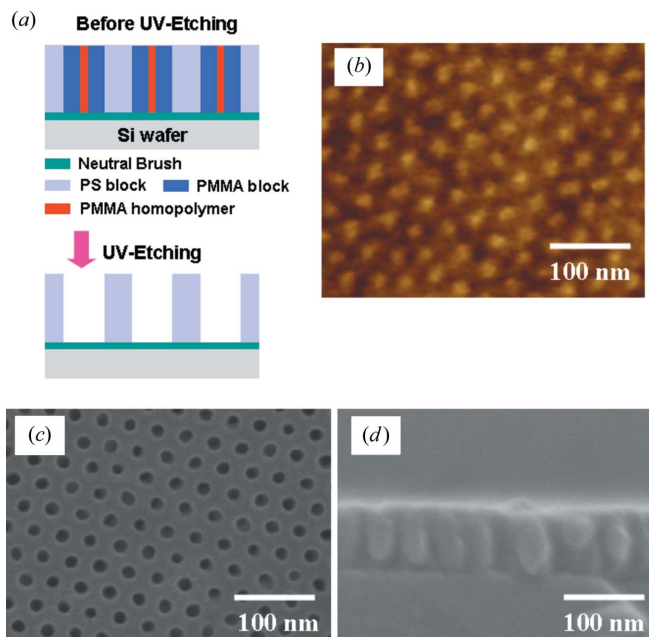


**Figure 2**

(*a*) Procedure for preparing a thin film of a PS-*b*-PMMA/PMMA mixture on a silicon substrate coated with PS-*r*-PMMA; (*b*) AFM surface image of an 80.0 nm thick film on a silicon substrate before UV-etching; (*c*) FE-SEM top and (*d*) cross section images of the film after UV-etching.

film thickness was larger than  $\sim 50$  nm (Jeong *et al.*, 2004). Fig. 2(*b*) shows a representative AFM image of a thin film of the PS-*b*-PMMA/PMMA mixture, which provides the surface topography of the mixture film but does not enable the determination of the morphological structure within the film. As can be seen in Fig. 2(*b*), the minor component in the surface appears as bright spots. In the mixture with the PMMA homopolymer, the PMMA block is the minor component by volume. Thus the bright spots correspond to the phase-separated PMMA phase, and the dark areas correspond to the PS phase. The thin films were further examined with field-emission scanning electron microscopy (FE-SEM), but the FE-SEM measurements could not provide any surface topography information. Fig. 2(*c*) displays a representative FE-SEM image of the surface of a UV-etched PS-*b*-PMMA/PMMA film, and Fig. 2(*d*) shows a representative FE-SEM image of a cross section of a UV-etched film with a thickness of 80 nm. These FE-SEM images indicate that the phase-separated PMMA microdomains in the mixture film were selectively removed by the UV-etching process, resulting in templated cylindrical nanopores which are oriented along the out-of-plane axis. However, these FE-SEM analyses do not provide detailed information about the size (*i.e.* radius and length) and size distribution of the cylindrical nanopores in the templated film, or about the electron density and porosity of the templated film.

Figs. 3(*a*) and 3(*b*) show representative two-dimensional GIXS patterns for thin PS-*b*-PMMA/PMMA films of two different thicknesses (28.5 and 78.8 nm) before UV-etching. Figs. 3(*c*) and 3(*d*) show the representative two-dimensional

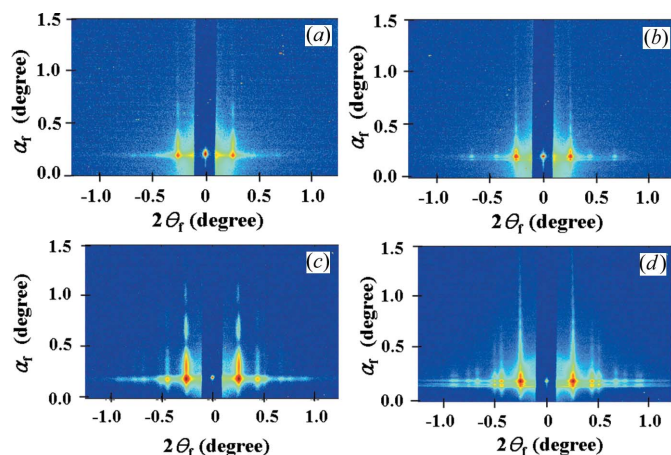


**Figure 3** Two-dimensional GIXS patterns measured at  $\alpha_f = 0.20^\circ$  for thin films of a PS-*b*-PMMA/PMMA mixture deposited on silicon substrates before and after UV-etching: (a) unetched 28.5 nm thick film; (b) unetched 78.8 nm thick film; (c) etched 25.0 nm thick film; (d) etched 86.1 nm thick film.

GIXS patterns of the thin films after UV-etching. As can be seen in Fig. 3, the etched films produce similar scattering patterns to those of the unetched films. However, the scattering patterns of the UV-etched films are much stronger in intensity and have clearer higher-order diffraction spots than those of the films before UV-etching. The significant difference between the scattering intensities of the films before and after etching is probably primarily due to the large electron contrast difference between the films. The difference between the electron densities of the phase-separated PMMA and PS domains in the unetched film is relatively small, whereas the difference between the electron densities of the templated nanopores and the PS matrix domains in the etched film is very large.

Fig. 4 shows the in-plane and out-of plane scattering profiles, which were extracted from the two-dimensional GIXS patterns in Fig. 3. The in-plane scattering profiles were extracted at  $\alpha_f = 0.19^\circ$  ( $q_z = 0.135 \text{ nm}^{-1}$ ), and the out-of-plane scattering profiles were extracted at  $2\theta_f = 0.26^\circ$  ( $q_{xy} = 0.185 \text{ nm}^{-1}$ ), where the first diffraction spot appeared. As can be seen in Fig. 4(a) (profiles A and B), the in-plane scattering profiles of the unetched films contain five diffraction spots with relative scattering vector lengths from the specular reflection position of  $1, 3^{1/2}, 4^{1/2}, 7^{1/2}$  and  $9^{1/2}$ ; the third and fifth spots are much weaker in intensity than the other spots. These diffraction spots are characteristic of a hexagonal structure, indicating that the phase-separated PMMA microdomains are packed hexagonally in the film plane.

However, the in-plane scattering profiles are quite different from the out-of-plane scattering profiles (Fig. 4b; profiles A and B). The out-of-plane scattering profiles mainly consist of oscillations. These profiles resemble the specular X-ray reflectivity profiles of thin films, which are modulated by Kiessig fringes (Bolze *et al.*, 2001). These fringes generally appear because of interference between the X-ray beams reflected from the film surface and those reflected from the film/substrate interface, namely the standing waves of the

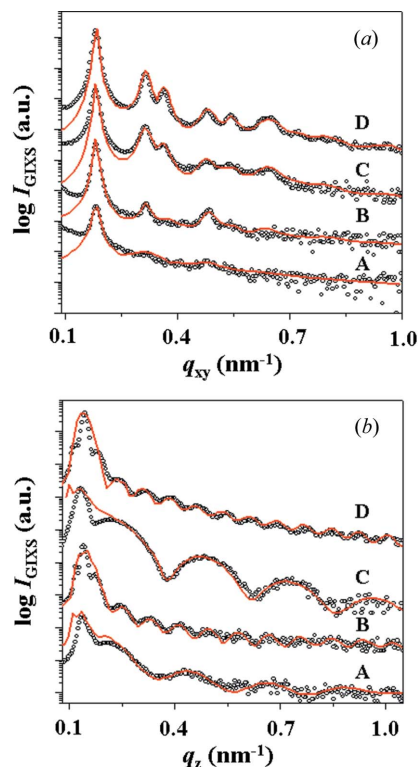


**Figure 4** (a) In-plane GIXS profiles extracted along the  $q_{xy}$  direction at  $\alpha_f = 0.19^\circ$  ( $q_z = 0.135 \text{ nm}^{-1}$ ) and (b) out-of-plane GISAXS profiles extracted along the  $q_z$  direction at  $2\theta_f = 0.26^\circ$  ( $q_{xy} = 0.185 \text{ nm}^{-1}$ ) from the two-dimensional GIXS patterns of thin films before and after UV-etching: (A) unetched 28.5 nm thick film; (B) unetched 78.8 nm thick film; (C) etched 25.0 nm thick film; (D) etched 86.1 nm thick film. The symbols are for the measured data, and the solid lines were obtained by fitting the data with the GIXS formula.

X-ray beam within the thin film. The film thickness can be estimated from the periodicity of the Kiessig fringes. The amplitude of Kiessig fringes is often modulated at a lower frequency if there is layer structure within the film. Low-frequency modulation is not present in the out-of-plane scattering profiles in Fig. 4(b). Furthermore, the out-of-plane scattering profiles show that no features characteristic of hexagonally packed PMMA microdomains lie on the out-of-plane axis, whereas such features are observed in the in-plane scattering profiles. These results indicate that the PMMA microdomains formed in the films are preferentially oriented perpendicular to the film plane and occupy the whole film thickness; in other words, the phase-separated PMMA microdomains are formed in the films with cylindrical shapes and heights comparable to the film thickness, and are oriented along the out-of-plane axis.

The etched films produce similar in-plane scattering profiles to those of the unetched films. However, the in-plane scattering profiles of the etched films contain seven clear diffraction spots, including the five spots observed in the unetched films, with relative scattering vector lengths from the specular reflection position of  $1, 3^{1/2}, 4^{1/2}, 7^{1/2}, 9^{1/2}, 12^{1/2}$  and  $13^{1/2}$  (Fig. 4a; profiles C and D). The out-of-plane scattering profiles of the etched films (Fig. 4b; profiles C and D) are also similar

**Table 1**  
Structural and property characteristics of thin films of the PS-*b*-PMMA/PMMA mixtures before and after UV-etching.

Sample	Structural parameters					Properties			
	$r^\dagger$ (nm)	$L^\ddagger$ (nm)	$\bar{R}^\S$ (nm)	$\sigma_R^\ddagger$ (nm)	$d_{sp}^{\dagger\dagger}$ (nm)	$g^{\ddagger\ddagger}$	$\alpha_c^{\S\S}$ ( $^\circ$ )	$\rho_{e,f}^{\P\P}$ ( $\text{nm}^{-3}$ )	$P_e^{\dagger\dagger\dagger}$ (%)
Before etching									
Film-1	28.5	28.5	11.0	3.01	34.0	0.053	0.156	348	–
Film-2	78.8	78.8	11.4	3.00	34.0	0.048	0.156	348	–
After UV-etching									
Film-3	25.0	25.0	11.8	2.95	34.0	0.040	0.136	265	25.3
Film-4	86.1	86.1	11.7	2.90	34.0	0.036	0.135	261	26.6

$^\dagger$  Film thickness measured by X-ray reflectivity and spectroscopic ellipsometry.  
 $^\ddagger$  Length of the cylindrical pores.  $^\S$  Pore radius determined from the peak maximum of the radius  $r$  and the number distribution of pores.  $^\ddagger$  Standard deviation of the pore radius.  $^{\dagger\dagger}$  Center-to-center distance of the cylindrical pores ( $d$ -spacing of the hexagon).  $^{\ddagger\ddagger}$  Paracrystal distortion factor.  $^{\S\S}$  Critical angle of the film determined from the out-of-plane GIXS profile.  $^{\P\P}$  Electron density determined from the critical angle of the film.  $^{\dagger\dagger\dagger}$  Porosity estimated from the electron density of the film with respect to the electron density of PS.

to those of the unetched films, but the oscillations are much more enhanced in the etched films. These results indicate that the hexagonal packing of the vertically oriented PMMA cylinders formed in the films is maintained throughout the UV-etching process, and that their removal leaves cylindrical nanopores.

Taking into account information obtained from the qualitative microscopy and GIXS analyses above, we attempted to analyze quantitatively the measured GIXS data. By analyzing the scattering data with the GIXS formula [equation (1)], we examined all possible scattering models (sphere, disc, cylinder *etc.*) of the scattered intensity from the microdomains (or their templated nanopores) in the films, and found that the most suitable scattering model was that for a hexagonal paracrystal lattice of cylinders. As shown in Fig. 4, the GIXS formula [equation (1)] for a hexagonal paracrystal lattice of cylinders can be used to fit both the in-plane scattering profiles and the out-of-plane scattering profiles of the films before and after UV-etching. From the quantitative analysis of the scattering data using the GIXS theory described above, the important structural parameters, namely cylinder shape, radius and radius distribution, length, center-to-center distance, orientation, degree of packing order, position distortion factor, electron density and porosity, were precisely determined and are summarized in Table 1. These structural details provide important information about the microdomains formed in the thin PS-*b*-PMMA/PMMA films and the templated pores as follows.

First, the lengths of the cylindrical PMMA microdomains formed in the film are equivalent to the film thickness. For films of 28.5–78.8 nm thickness, the PMMA cylinders have radii in the range 11.0–11.4 nm with a radius distribution of 3.00–3.01 nm. These results confirm that the cylindrical PMMA microdomains are preferentially formed perpendicular to the film plane, *i.e.* they occupy the whole film thickness, and that the formation of these PMMA cylinders in the films occurs for film thicknesses in the range 28.5–78.8 nm.

Second, the lengths of the cylindrical nanopores templated in the UV-etched films are equivalent to the film thickness. The radii (11.7–11.8 nm) of the templated cylindrical nanopores in the etched films are comparable with those (11.0–11.4 nm) of the PMMA cylinders in the unetched films. The radius distribution (2.90–2.95 nm) of the templated cylindrical nanopores is also comparable with that (3.00–3.01 nm) of the PMMA cylinders in the unetched films. These results indicate that the UV-etching process effectively and selectively etched the cylindrical PMMA microdomains through the whole film thickness, resulting in cylindrical nanopores in the film.

Third, both the vertically oriented PMMA cylinders in the film and their templated cylindrical nanopores were found to assemble laterally to form a hexagonal paracrystal lattice with paracrystals that are rather randomly packed in the film plane. Furthermore, each cylinder in the hexagonal paracrystal lattice has a distortion of the second kind, described by the  $g$  factor. The  $g$  factor of the cylinders was found to be very small (0.036–0.053), indicating that the positional disorder of the cylinders in the hexagonal paracrystal lattice is very small. The  $g$  factor for the cylindrical PMMA microdomains in the unetched film is larger than that for the templated nanopores in the etched film. This difference between the  $g$  factors is possibly due to the difference between the contrasts of the interfaces of the PMMA cylinders and their cylindrical nanopores with the PS matrix in the films; the interface of the PMMA cylinders with the PS blocks might be somewhat diffuse because of the interconnectivity of the two phases. In contrast, the cylindrical air-filled nanopores have a very sharp interface with the PS matrix.

Fourth, the critical angle of each thin film ( $\alpha_{c,f}$ ) was determined from the analysis of its out-of-plane scattering profile.  $\alpha_{c,f}$  was found to be  $0.156^\circ$  for the unetched films and  $0.135$ – $0.136^\circ$  for the etched films (Table 1).  $\alpha_{c,f}$  is directly related to the electron density of the film ( $\rho_{e,f}$ ):  $\rho_{e,f} = \pi\alpha_{c,f}^2/r_e\lambda^2$ , where  $r_e$  is the classical radius ( $2.818 \times 10^{-15}$  m) of the electron and  $\lambda$  is the wavelength of the X-ray beam (Bolze *et al.*, 2001). Using this relationship, the electron densities of the thin films were estimated from the  $\alpha_{c,f}$  values:  $\rho_{e,f}$  is  $348 \text{ nm}^{-3}$  for the unetched films and  $261$ – $265 \text{ nm}^{-3}$  for the etched films (Table 1).

Fifth, the porosities  $P_e$  of the UV-etched films can be estimated from the electron densities  $\rho_{e,f}$  with respect to those of the unetched films. The obtained  $P_e$  values are in the range 25.3–26.6% (Table 1), which are in good agreement with the volume percent (26.7%) of the PMMA phase in the films before UV-etching.

Finally, by using these structural parameters, we attempted to calculate the two-dimensional GIXS patterns using the GIXS formula for the model of the hexagonal paracrystal lattice of cylinders. The results are presented in Fig. 5. As can be seen in the figure, the calculated two-dimensional GIXS patterns for an unetched film and an etched film are in good agreement with their measured scattering patterns (Fig. 3), confirming that the measured GIXS patterns were successfully analyzed.

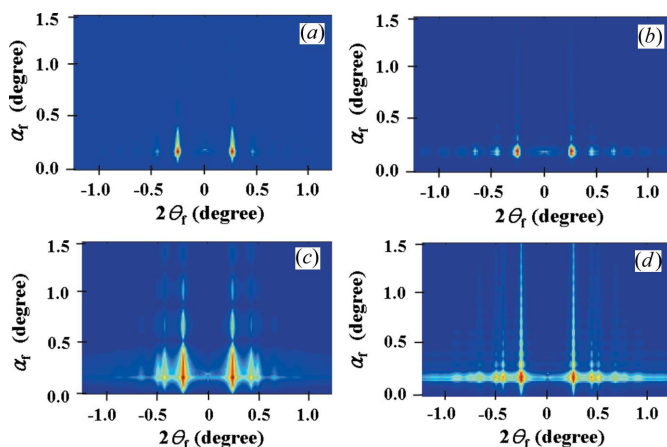


**Figure 5**  
Two-dimensional GIXS patterns calculated for thin films of a PS-*b*-PMMA/PMMA mixture deposited on silicon substrates before and after UV-etching: (a) unetched 28.5 nm thick film; (b) unetched 78.8 nm thick film; (c) etched 25 nm thick film; (d) etched 86.1 nm thick film. In these calculations, the structural parameters and electron densities in Table 1 were used; the hexagonally packed cylindrical microdomains and templated nanopores were assumed to be perfectly oriented perpendicular to the film plane.

### 5. Conclusions

In this study we applied a GIXS formula for hexagonally packed structures with orientation in thin films supported on substrates. A comprehensive numerical analysis using the GIXS formula combined with a scattering theory of the hexagonally packed structures with orientation was performed. Two-dimensional GIXS measurements were successfully conducted for nanostructured thin films of a mixture of PS-*b*-PMMA diblock copolymer and PMMA homopolymer on silicon substrates and their templated nanopores. We demonstrated a quantitative analysis of the measured scattering data by the combined GIXS formula, and obtained detailed structural information (*i.e.* shape, size and size distribution, orientation, and packing order) as well as the properties (electron density and porosity) that are not easily obtainable using conventional techniques such as TXS, TNS, AFM, TEM and SEM.

This study was supported by the Korea Science and Engineering Foundation (National Research Lab Program, National Creative Research Initiative Program and Center for Integrated Molecular Systems) and by the Ministry of Education (BK21 Program). Synchrotron GIXS measurements at the Pohang Accelerator Laboratory were supported by the Ministry of Science and Technology and the POSCO.

### References

Bolze, J., Kim, J., Huang, J.-Y., Rah, S., Youn, H. S., Lee, B., Shin, T. J. & Ree, M. (2002). *Macromol. Res.* **10**, 2–12.

Bolze, J., Ree, M., S., Y. H., Chu, S. H. & Char, K. (2001). *Langmuir*, **17**, 6683–6691.  
 Busch, P., Rauscher, M., Smilgies, D.-M., Posselt, D. & Papadakis, C. M. (2006). *J. Appl. Cryst.* **39**, 433–442.  
 Busson, B. & Doucet, J. (2000). *Acta Cryst.* **A56**, 68–72.  
 Chung, B., Choi, M., Ree, M., Jung, J. C., Zin, W. C. & Chang, T. (2006). *Macromolecules*, **39**, 684–689.  
 Fournet, G. (1951). *Bull. Soc. Fr. Mineral.* **74**, 37–39.  
 Hashimoto, T., Kawamura, T., Harada, M. & Tanaka, H. (1994). *Macromolecules*, **27**, 3063–3072.  
 Holy, V., Pietsch, U. & Baumbach, T. (1999). *High-Resolution X-ray Scattering from Thin Films and Multilayers*. Berlin: Springer-Verlag.  
 Hosemann, R. & Bagchi, S. N. (1962). *Direct Analysis of Diffraction by Matter*. Amsterdam: North-Holland.  
 Jeong, U., Ryu, D. Y., Kho, D. H., Kim, J. K., Goldbach, J. T., Kim, D. H. & Russell, T. P. (2004). *Adv. Mater.* **16**, 533–536.  
 Kim, Y., Cook, S., Tuladhar, S. M., Choulis, S. A., Nelson, J., Durrant, J. R., Bradley, D. D. C., Giles, M., McCulloch, I., Ha, C.-S. & Ree, M. (2006). *Nat. Mater.* **5**, 197–203.  
 Lakshmi, B. B. & Martin, C. R. (1997). *Nature (London)*, **388**, 758–760.  
 Lee, B., Oh, W., Hwang, Y.-T., Park, Y.-H., Yoon, J., Jin, K. S., Heo, K., Kim, J., Kim, K.-W. & Ree, M. (2005). *Adv. Mater.* **17**, 696–701.  
 Lee, B., Oh, W., Yoon, J., Hwang, Y., Kim, J., Landes, B. G., Quintana, J. P. & Ree, M. (2005). *Macromolecules*, **38**, 8991–8995.  
 Lee, B., Park, I., Yoon, J., Park, S., Kim, J., Kim, K.-W., Chang, T. & Ree, M. (2005). *Macromolecules*, **38**, 4311–4323.  
 Lee, B., Park, Y.-H., Hwang, Y.-T., Oh, W., Yoon, J. & Ree, M. (2005). *Nat. Mater.* **4**, 147–150.  
 Lee, B., Shin, T. J., Lee, S. W., Yoon, J., Kim, J. & Ree, M. (2004). *Macromolecules*, **37**, 4174–4184.  
 Lee, B., Yoon, J., Oh, W., Hwang, Y.-T., Heo, K., Jin, K. S., Kim, J., Kim, K.-W. & Ree, M. (2005). *Macromolecules*, **38**, 3395–3405.  
 Meneou, K., Tsai, C. L., Zhang, Z. H. & Cheng, K. Y. (2005). *J. Vac. Sci. Technol. B*, **23**, 1232–1235.  
 Miller, S. A., Young, V. Y. & Martin, C. R. (2001). *J. Am. Chem. Soc.* **123**, 12335–12342.  
 Omote, K., Ito, Y. & Kawamura, S. (2003). *Appl. Phys. Lett.* **82**, 544–546.  
 Park, C., Yoon, J. & Thomas, E. L. (2003). *Polymer*, **44**, 6725–6760.  
 Park, I., Lee, B., Ryu, J., Im, K., Yoon, J., Ree, M. & Chang, T. (2005). *Macromolecules*, **38**, 10532–10536.  
 Pedersen, J. S. (1994). *J. Appl. Cryst.* **27**, 595–608.  
 Pedersen, J. S. (1997). *Adv. Colloid Interf. Sci.* **70**, 171–210.  
 Ree, M. & Ko, I. S. (2005). *Phys. High Tech.* **14**, 2–7.  
 Sakurai, S., Irie, H., Umeda, H., Nomura, S., Lee, H. H. & Kim, J. K. (1998). *Macromolecules*, **31**, 336–343.  
 Sinha, S. K., Sirota, E. B., Garoff, S. & Stanley, H. B. (1988). *Phys. Rev. B*, **38**, 2297–2311.  
 Thurn-Albrecht, T., Schotter, J., Kastle, A., Emley, N., Shibauchi, T., Krusin-Elbaum, L., Guarini, K. W., Black, C. T., Tuominen, M. T. & Russell, T. P. (2000). *Science*, **290**, 2126–2129.  
 Tolan, M. (1999). *X-ray Scattering from Soft Matter Thin Films*. Berlin: Springer-Verlag.  
 Wang, X., Summers, C. J. & Wang, Z. L. (2004). *Nano Lett.* **4**, 423–426.  
 Wu, Y. Y., Livneh, T., Zhang, Y. X., Cheng, G. S., Wang, J. F., Tanag, J., Moskovits, M. & Stucky, G. D. (2004). *Nano Lett.* **4**, 2337–2342.  
 Yang, S. Y., Ryu, I., Kim, H. Y., Jang, S. K., Kim, J. K. & Russell, T. P. (2006). *Adv. Mater.* **18**, 709–712.  
 Yu, C.-J., Kim, J., Kim, K.-W., Kim, G.-H., Lee, H.-S., Ree, M. & Kim, K.-J. (2005). *J. Kor. Vac. Soc.* **14**, 138–142.